Experience with the UKIRT InSb Array Camera

Ian S. McLean Mark M. Casali Gillian S. Wright Colin Aspin

Joint Astronomy Centre, 665 Komohana Street, Hilo, Hawaii 96720

Abstract

The cryogenic infrared camera, IRCAM, has been operating routinely on the 3.8 m UK Infrared Tele scope on Mauna Kea, Hawaii for over two years. The camera, which uses a 62×58 element Indium Antimonide array from Santa Barbara Research Center, was designed and built at the Royal Observatory, Edinburgh which operates UKIRT on behalf of the UK Science and Engineering Research Council. Over the past two years at least 60% of the available time on UKIRT has been allocated for IRCAM observations. In this paper we describe some of the properties of this instrument and its detector which influence astronomical performance, discuss observational techniques and illustrate the power of IR arrays with some recent astronomical results.

1 INTRODUCTION

A near infrared imaging system called IRCAM has been in use at the 3.8 m United Kingdom Infrared Telescope since September 1986, and a second camera was introduced toward the end of 1988. Both of these cryogenic imaging systems are "facility" or "common-user" instruments. In competitive scientific proposals, IRCAM has been requested as the instrument of choice for 60–70% of the total telescope time, and is virtually always available as a backup for other instruments. Both cameras use the 62×58 pixel Indium Antimonide (InSb) Direct Readout (DRO) array manufactured by Santa Barbara Research Center (SBRC). In an evolutionary process, several different detectors have been used and evaluated over the past two years in a wide range of ground-based astronomical applications, and a considerable amount of observational experience has been gained.

Naturally, the advent of near infrared imaging systems has led to what might be termed an explosion in *infrared picture-taking*! The ease with which seeing-limited images of a wide range of objects — often invisible at optical wavelengths — could be obtained, especially in non-photometric weather conditions, has led to a huge increase in morphological studies, infrared surveys and studies in which much new insight is gained even if no attempt is made to calibrate the observed brightness levels with high accuracy. Gradually, that situation has been changing to include precise astronomical photometry as more experience is gained on how to calibrate infrared array data. In fact, it is remarkable how quickly infrared arrays have been put to use as precise photometric tools. Undoubtedly, experience carried over from work with optical CCDs has helped considerably.

In this paper we describe some of the properties of the 62×58 InSb detector which influence astronomical performance, describe our observational techniques and illustrate the progress in ground-based IR astronomy with recent results from UKIRT.

2 THE CAMERA SYSTEM

Various aspects of the design and the performance of IRCAM are described in detail elsewhere [1,2,3] so only a summary of major characteristics are given here.

Optically, IRCAM employs un-cooled gold-coated mirrors to collimate the f/36 beam (at 1.53″/mm) from the telescope before it passes through the calcium fluoride window of a vacuum chamber within which is housed the cryogenic camera assembly; the low temperatures are achieved by attaching the vacuum chamber to a large Oxford Instruments LHe/LN_2 dewar. Four liters of liquid helium provide a hold-time of well over two days. (More recently, lab tests with a closed-cycle cooler have demonstrated that this approach is also viable.) Optical re-imaging is performed by one of three cold (77 K) lenses of AR-coated zinc selenide, selected prior to cool-down, which transfer the telescope focal plane image onto the detector array at approximately f/7.2, f/3.6 or f/1.8. Filters are placed in the collimated beam near the position of the Lyot-stop (an image of the entrance pupil). The instrument is a side-looking construction fed by a 45-degree inclined dichroic mirror near the UKIRT f/36 focus, and is one of a cluster of four semi-permanently mounted instruments.

Drive electronics (clock drivers, bias supplies and signal processing circuits), a temperature controller and a two-channel 15 bit A/D unit are located alongside the dewar; clock and bias/signal lines are separated. There is an internal preamp with a gain of 5. A hardware sequencer/computer interface employing Programmable Logic Arrays is located nearby on the mirror cell. The sequencer and an array timing logic unit (supplied by SBRC) are controlled by an LSI 11/23+ microprocessor running DEC MicroPower Pascal software. Also on the mirror cell is a motor-control unit with an IEEE 488 bus to drive the three 5-phase stepper motors used in IRCAM. Digital data from the A/D unit is transferred by a parallel link to a remote LSI 11/73 which acts as a buffer computer capable of "coadding" many frames or exposures before transferring the final image to the UKIRT MicroVax II.

At present, three image scales are available with IRCAM 1 and 2 namely, 0.63, 1.25 and 2.4″/pixel, giving fields-of-view of 39×36.5″, 77.5×72.5″ and about 135″ diameter; the wide field mode is limited by the size of the collimator mirror and the desire to minimise its tilt angle. IRCAM 2 contains a 10% oversized cold-stop, whereas IRCAM 1 is fitted with a special slightly undersized Lyot-stop mask. A choice of broad and narrow bandpass filters are contained in IRCAM's two 10-position filter wheels. In addition to the standard JHKL filters there are 1% bandwidth filters for the Brackett alpha and Brackett gamma lines of hydrogen, the v=1-0 S(1) transition of molecular hydrogen, CO bands at 2.30 μm, ice band at 3.08 μm and the emission feature at 3.28 μm associated with very small grains. Also available is a filter for the 1.644 μm [FeII] line and several regions of continuum.

Other instrumentation can also be used with IRCAM. For example, a piezoelectrically scanned Fabry-Perot etalon, manufactured by Queensgate Instruments, can be placed in the collimated beam immediately outside the dewar window to give an imaging mode with spectral resolving powers in excess of 3500. There is also an infrared polarimeter option (IRPOL) employing a rotatable halfwave plate above the UKIRT dichroic mirror and cold polarizers internal to IRCAM. Recently a slitless "grism" mode providing about 1% spectral resolution across the K-band has been installed, and in addition, a coronagraph mode — developed in collaboration with Ben Zuckerman at UCLA — has been used successfully.

IRCAM is a highly-automated, computer-driven instrument with a very extensive suite of software. Control is from a console/workstation in the UKIRT Control Room either by use of a simple menu or by typing a few keywords which represent command procedures; each procedure prompts the user for required input. For example,

OBS(erve) will request all parameters necessary to set up an observation and store the data;

GO will initiate a simple STARE or CHOP observation;

GODARK will obtain a dark/bias pair and return to the original setup;

GOJHK will carry out a sequence of observations in each passband;

SHOW will enable the resulting image to be displayed;

MAG will return zeropoints/magnitudes of a star;

FINISH will terminate the observing session.

All high-level software is written in FORTRAN, and a great deal of image processing power is available on-line. Instrument status is shown on a monitor at all times and images can be displayed immediately on a high resolution color image display screen with hardcopy facilities. Complex data reduction, such as median filtering of sky flat-fields, piecing together mosaics or deriving polarization parameters, can be carried out while integrations are in progress. There are on-line "magnitude" programs using mean zeropoints, and there are many "procedures" which can be called to execute a repetitive or tedious sequence, including control of the telescope for mapping. Sky conditions (mean signal level per coadd and noise) can be monitored with selectable pixels on the array and displayed on the status monitor. At the end of the night the data stored on the summit disk are also transferred to the sea-level facility, linearised and two copies backed-up onto magnetic tape. Tapes are provided in FITS format or in Vax backup format.

Despite the complexity of the instrument, visitors need only learn a few commands to take data and assess its quality. In addition, more sophisticated image processing software in Hilo allows the user to leave with publication quality hardcopy from either the Seiko D-Scan colour paper unit or the Matrix instruments colour film unit.

3 DETECTOR CHARACTERISTICS AND PERFORMANCE

The SBRC detector itself has been described in detail elsewhere [4,5]. Briefly, the detector is a thinned backside-illuminated "hybrid" formed from an array of reversed-biased InSb photodiodes bonded by indium "bump" interconnects to an array of silicon MOSFET devices thereby associating a Source Follower amplifier to each detector. The silicon Read Out Integrated Circuit (ROIC) is called the CRC-228 Direct Read Out or "DRO" and was developed by the Hughes Micro-Electronics Center in Carlsbad, California. Each source follower MOSFET or "unit cell" can be (randomly) accessed using an on-chip multiplexing scheme. Hence the term Direct Read Out. Photocharge is accumulated on the combined capacitance (C) of the junction of the reverse-biased diode (quoted as 0.65 picofarads by SBRC for the latest devices; for earlier devices the value was about 1.0 pF), the gate of the source follower FET and the indium bump contact (about 0.1 pF together). The potential on this storage capacitance can be reset through an FET switch to a certain "reset" level although in practice the actual level or "pedestal" after reset is uncertain - the so-called *kTC noise*. Odd and even numbered pixels are read out separately via two output amplifiers. Saturation or "full-well" condition (CV_{bias}/e) of the device corresponds to a fully de-biased detector; the detector is still light sensitive and does not bleed or bloom, but integration ceases.

In IRCAM, the 62×58 InSb detector is typically operated at a temperature of about 35 Kelvin to minimise any loss of quantum efficiency or DRO performance, while achieving acceptably low dark currents over most of the array; below 40 K dark current ceases to decrease exponentially. Operating parameters are given in Table 1.

To date, nine SBRC InSb arrays have been received and operated. Of these, one had a blown gate (used to control surface charge) and was therefore insensitive, three incorporated a batch of high-doped

Parameter	Value
Detector Bias	-250 mV
Gate Voltage (typical)	-1.0 V
V_{DD}	<1.5 V
Clocks	0–5.0 V
Detector Temperature	35 K
System Gain (typical)	30 e^-/ADU
kTC noise	~120 e^-
Readout Rate (normal)	130 ms/frame

Table 1: Operating Conditions for SBRC 62×58 Arrays in IRCAM

InSb which failed to retain quantum efficiency at low operating temperatures, and five were low-doped InSb arrays with generally good performance characteristics. Devices FPA118, FPA175 and FPA180 all operate with gate voltages about 2 V *less* negative than their predecessors. A summary of the characteristics of four of our detectors is given in Table 2.

Parameter	FPA061	FPA118	FPA175	FPA180
QE	all in range 50–70% over 1–5 μm			
Readout Noise	450 e^-	500 e^-	480 e^-	400 e^-
Dark Current	150 e^-/s	120 e^-/s	150 e^-/s	60 e^-/s
Full Well	all about 1 x 10^6 e^-			
Bad pixels	112(3%)	25(0.7%)	15(0.4%)	75(2%)

Table 2: Performance figures for SBRC 62×58 InSb Arrays

The noise values are obtained under actual observing conditions using the *reference-to-reset* or "double-correlated sampling" mode. For FPA118 and earlier devices, an anti-reflection coating with a peak near 3 μm was used on the InSb; later devices have a coating which peaks near 1.7 μm. Bad pixels are usually of two types, "dead" or "hot"; the latter pixels saturate instantly.

In the IRCAM system the detector is maintained in a "standby" mode in which it is continuously read out until an integration or "exposure" is requested. At the end of the timed integration period the photocharge is read out in "burst mode" and digitised to 15 bits. IRCAM may be operated in conjunction with the UKIRT chopping secondary mirror, but in general we opt to use STARE mode.

Detectors are normally baked in a clean vacuum oven at 80–90 C for 24 hours before installation into the camera and every effort is made to avoid subsequent contamination with water vapour. If this is not done an unstable, "ring-like" region of high "dark" current will be observed spreading inwards from the edge of the array. For each device a *gate voltage* is derived which minimises dark current over most of the array; we have generally found that in our cryostats this voltage settles out about (2.0 ± 0.5) Volts more negative than recommended in the SBRC data sheet ;the gate voltage exhibits hysteresis. Some devices show a slight "after-image" effect following exposure to high flux levels. The output FET drain voltage (V_{DD}) must be reduced considerably (less than 1.5 V) to minimise light emission effects in one corner of the array and V_{rstuc} can have a strong influence on linearity performance. Many of the early chips exhibited spurious light-emitting problems associated with multiplexer faults.

4 CAMERA PERFORMANCE

The camera, or more precisely, the system performance — including the telescope — is generally background-limited. The system efficiency, that is the product of QE (η) and total transmission (τ) of all optics, is about 20% and extraneous background entering the dewar is controlled and constrained as much as possible by a series of baffles and cold-stops, and by careful mechanical design. Observed backgrounds are reasonably consistent with detailed models [6] and yield typically 2,000 e^-/s/pixel in the J band and 10,000 e^-/s/pixel in the K band with 0.6″ pixels; the J band filter is from Barr Associates and the K filter is from OCLI. Because of the large collecting aperture of UKIRT and the minimum integration time of 50 ms, we are unable to use the standard L′ filter at 3.8 μm, but various narrower bands are possible. In the Fabry-Perot imaging spectroscopy mode the etalons are external to the cryostat, i.e. at dome temperature, and consequently the background is no less than that expected for the narrow-band blocking filter.

For a readout noise of 500 e^- rms the accumulated photocharge must exceed 250,000 e^- before the system begins to become background-limited. This is equivalent to about 25% of full well capacity. Exposure times "on-chip" are optimised to avoid detector saturation yet give background-limited operation by filling the wells to at least 75% full; values range from 50 ms at the longest wavelengths to ten minutes or more with narrow bands at the shorter wavelengths.

4.1 Calibrations

Several corrections to "raw" images are required including (dark current + bias level) subtraction, flat-fielding and non-linearity. The success of these will depend on the stability of the detector system and on the observing strategy used. It is important to realise that the observing strategy can vary considerably from one case to the next depending on the scientific goal, but it is nevertheless true that it is rare to find anyone spending *too much* time on calibrations.

4.1.1 Non-linearity.

The SBRC InSb DRO array is inherently non-linear in its response to photon illumination due to the dependence of the capacitance (C) on the value of the reverse bias voltage which itself is a decaying function of time due to photocharge and/or dark current (see also ref. 6 and the presentation by M. McCaughrean). In other words, high photon fluxes give smaller output signals (in A/D units) than would be expected from a linear extrapolation from signal outputs associated with much lower illumination levels. The magnitude of the effect in all practical circumstances is less than 10% (typically around 8% at 75% of full well) and easily calibrated as shown in Figure 1. A fifth-order polynomial fit to the linearity curve is used to correct "bias-subtracted" images as a first step in data-processing; linearity is restored to an accuracy of about 0.1%.

4.1.2 Dark current and bias.

The "bias" level is the electronic offset or signal obtained for an extremely short exposure with no incident illumination whatsoever. The latter condition is achieved with a "dark slide" at 77 K. Some devices show a large-scale gradient in the bias level along rows, others are largely random. Since the SBRC array is a two-channel output device, odd and even numbered columns may have slightly different levels. This effect can be trimmed-out but is in anycase removed by bias subtraction. A "dark current" frame is obtained in the same way but with a much longer exposure. Dark current is spatially non-uniform and a non-linear function of the reverse bias applied to the detector, therefore it must be carefully determined when it is an appreciable fraction of the background signal — *e.g.* narrow band

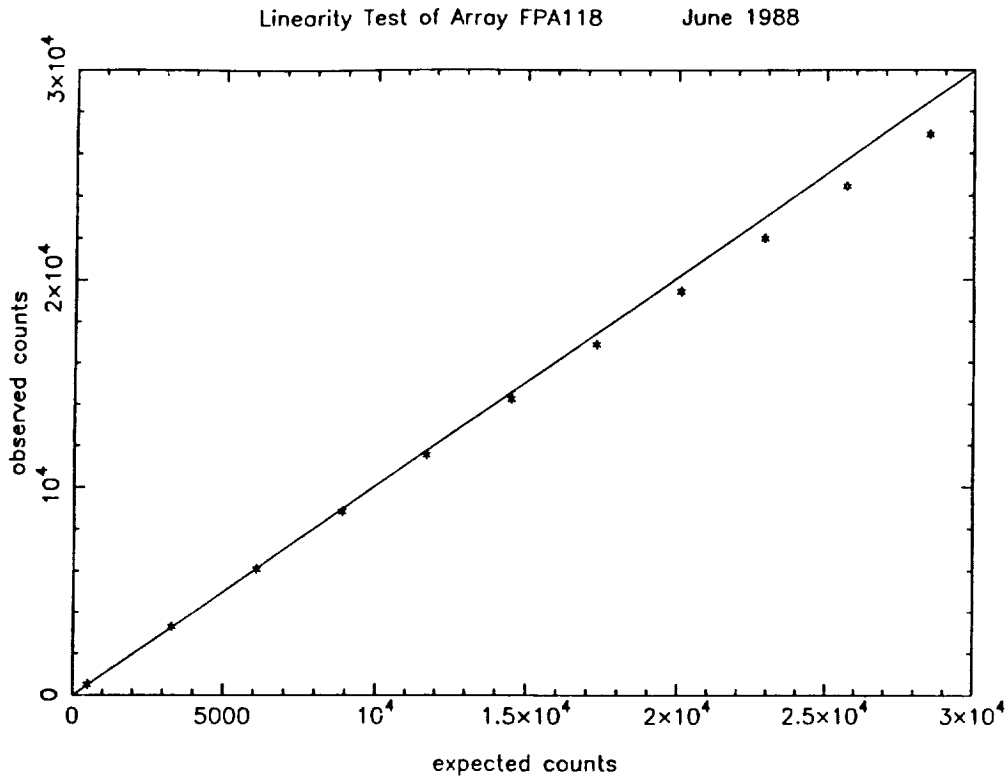

Figure 1: A plot of the output signal counts versus the true input signal counts for the SBRC 62×58 array. The departure from linearity is easily calibrated.

imaging at short wavelengths. At temperatures around 35K the dark current is relatively small and only weakly temperature-sensitive. Near the edges of an array however, the dark current can rise sharply and is very sensitive to gate voltage; small drifts can then lead to "edge-effects" in the image.

4.1.3 Flat-fielding.

Spatial variations in the response of the detector to light are calibrated by dividing by a uniformly illuminated scene — a "flat-field" — of the same color, after dark subtraction (see also more detailed discussion by McCaughrean). That is, the basic algorithmn most often used is

$$\frac{\text{Object frame - dark frame}}{\text{Flatfield frame - dark frame}}$$

The *same* dark frame should be used for object frame and flat-field frame since, to first order, this suppresses the effect of a small drift in dark current level and the signal-to-noise is barely affected if the dark current exhibits good uniformity. We have found that flat-fields are best derived from multiple observations of relatively "blank" sky. Since at some level there will always be sources in the blank sky area, the best technique is to take many images (>5) with the telescope pointing to a slightly different place (by $\sim 5''$ typically), normalise these and calculate the median value for every pixel. This procedure produces a very clean "master" flat-field. For almost empty fields the object frames and the skyflats are one-and-the-same. It is also advantageous to use a running-median flat-field when coadding an extensive data set obtained over many hours; the particular object frame being flattened by the median of the other frames should not be included in the median. With this technique the spatial

non-uniformities, of order 10–20%, can be easily reduced to much better than 0.1% and in an extended survey to very faint levels at 2.2 μm IRCAM has achieved a flat-field precision of 0.007%, by which we mean the *noise* on the mean sky level in the flat-fielded image.

Typical bias, dark and skyflat frames are shown in Figure 2. Regular off-setting to the sky to obtain flat-fields in cases where the primary frame is too crowded does, of course, double the observation time — making it the same as conventional IR photometry — but, for a given total observation time a 50:50 split gives the best signal-to-noise. Also, subtle shifts in the color of the skyflat with time, for instance, make this technique preferable to obtaining all the flats at the end of the night. Taking of such regular sky frames has a convenient and practical side-effect in that it becomes very easy to display (object - sky) differences for a quick-look and provides a means of estimating the temporal stability of the background.

4.1.4 Lamp calibrations.

Since IRCAM is used quite often with a Fabry-Perot interferometer, and now also with a grism, calibrations against an arc-lamp are required. These are basically of two types; wavelength calibration and phase shift. For the former the arc lamp is in focus in the focal plane and for the latter the lamp emission is uniformly diffused to produce a monochromatic flat field.

4.1.5 Polarization calibrations.

Instrumental polarization can be checked against unpolarized stars and position angle offsets from the equatorial system are calibrated against a reference polarizer and against highly polarized sources. There is a one magnitude loss in sensitivity in the IRPOL mode due almost entirely to the polarizer. Since the precision in the measurement of the percentage polarization is $\sigma_P \approx 70\% \times$ *photometric precision/frame* in the photon-noise-limited case, then very high signal-to-noise ratios in photometry are required for good polarimetry, typically 200:1. Good image registration is crucial in the calculation of accurate and reliable polarization. Users should also be aware of the need to remove polarized sky emission from their data (at the shorter near-IR wavelength) when the moon is bright especially if conditions are hazy.

4.2 Astronomical performance

In Table 3 we summarise the sensitivity or "limiting-magnitude" performance of IRCAM 1 in its high-resolution mode of 0.63″ per pixel which is well-matched to typical seeing conditions.

Scale	J	H	K	nbL
0.6″/pix	21.5	21.0	20.3	14.6 mags
	(3.82)	(3.89)	(4.70)	(419) μJy

Table 3: Sensitivity of IRCAM 1

The values are 3 sigma detections in 30 minutes expressed in equivalent magnitudes per square ″ and in μ Jansky. The center wavelengths of the JHKnbL set are respectively 1.26, 1.65, 2.2 and 3.6 μm; passbands are about 20% of the wavelength except for nbL which is 2%. For an object subtending 25 pixels (5×5) in the background-limited case the 3 sigma, 30 minute detection level is 19.1 at K.

Astronomical photometry with IR arrays is now a reality provided the same degree of care is taken as with single-channel photometers (software apertures of sufficient size, psf fitting, airmass corrections).

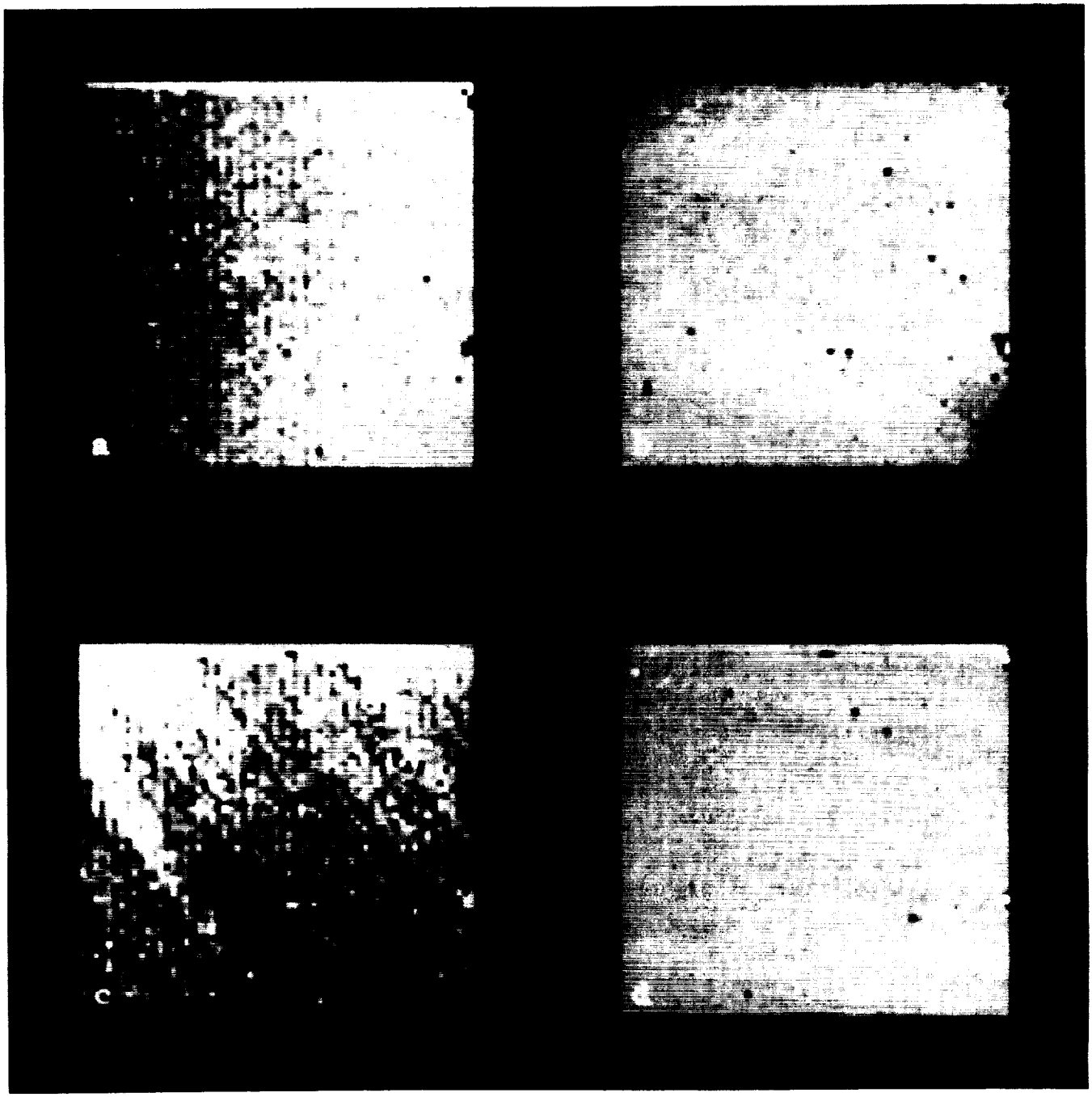

Figure 2: Four frames from a 62×58 InSb array from SBRC showing (a) Bias; (b) dark current; (c) flat-field response at K (2.2 μm); (d) the ratio of two flat-fields.

In a study of bright (K = 7) standard stars we achieved relative photometry between objects on the *same* frame to 0.003 mag (0.3%) and between objects on different frames the agreement was rarely worse than 0.03 mag (3%). Color corrections relative to the UKIRT InSb photometers seem to be small, as expected. For fainter objects and extended sources it becomes essential to have "sky on the frame". Observations of white dwarf stars at K=12–15 have given good agreement (3–5%) with the UKIRT photometers and faint sequences are currently being established as a side-effect of an extensive study of globular clusters.

5 RECENT RESULTS

Infrared imaging systems like IRCAM are now being used widely, in both hemispheres, and in diverse applications. Popular reviews have been given by McLean [7,8] and by Gatley et al. [9]. Progress has been very rapid since the pivotal workshop on *Infrared Astronomy with Arrays* held in Hilo, Hawaii in March 1987 [10]. A selection of some of the highlights from the UKIRT camera over the past two years are listed below.

5.1 Star forming regions

A complete, high resolution (seeing-limited) image of the high-mass star forming cluster in the Orion Nebula was obtained during commissioning of IRCAM 1 leading firstly to a Luminosity Function at 2.2 μm— a plot of the number of stars per unit magnitude interval — (see Figure 3)and then to a full, multi-color photometric study of over five hundred embedded stars [2,6]. The latest results, using Point Spread Function fitting with the DAOPHOT package, are described in the paper following this one.

Many other star forming regions have also been observed. A good example is the object Mon R2 IRS [24]. Figure 7c shows a composite J, H and K image of the region where the J-flux has been colour coded blue, the H-flux coded green and the K-flux coded red. This gives an immediate picture of the colour variations over the object which in this case are interpreted as a combination of emission, absorption and scattering.

In several cases the linear polarization of scattered light from deeply embedded sources has been used to locate the source and to distinguish it from a bright knots of nebulosity. An excellent example is the source GGD-27 [23] shown in Figure 4. The vector plot indicates that the brightest near-infrared source is *not* the illumination source for the nebula.

Many images have been obtained in the light of molecular hydrogen (H_2) emission of regions such as HH7-11 and DR21 which show clear evidence of "bow" shocks [11], and in S106 where the disruption of a placental cloud is observed [12].

5.2 Galaxies

Infrared images of a great many IRAS galaxies, AGNs and known interacting galaxies have been obtained with sufficient resolution to reveal the detailed morphology such as, multiple compact sources, bar-like features, connecting "arms" *etc.*, as well as provide surface brightness profiles.

We have also obtained the first high-resolution, completely-sampled infrared image of the giant spiral galaxy M51 at 2.2 μm (see Figure 5). Because the K light from a galaxy is dominated by light from red giant stars, which trace the distribution of the oldest and most massive stellar component, and because it is significantly less affected by dust than optical emission, such near-infrared images are ideal for the study of structure in nearby galaxies and for comparision with images at wavelengths dominated by other processes (*e.g.* HI, CO, HII, etc). Notice the absence of the striking dust lanes and obscuration in front of the companion galaxy which are seen in optical images. In the IR the companion is clearly seen

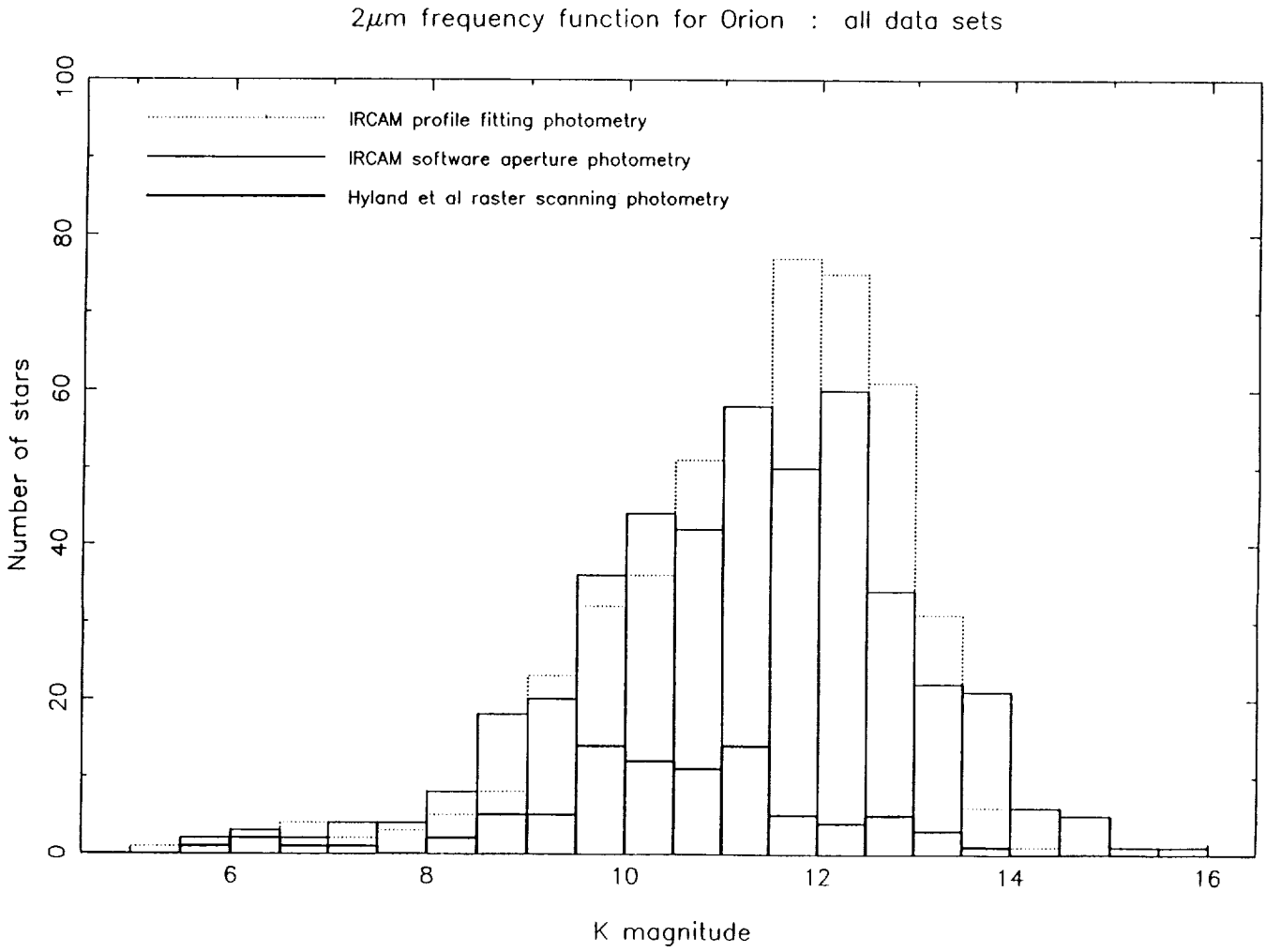

Figure 3: The frequency distribution of K magnitudes in the Orion Trapezium star cluster. If the sun were located at the distance of this cluster its K magnitude would be about 13. (Adapted from McCaughrean 1988).

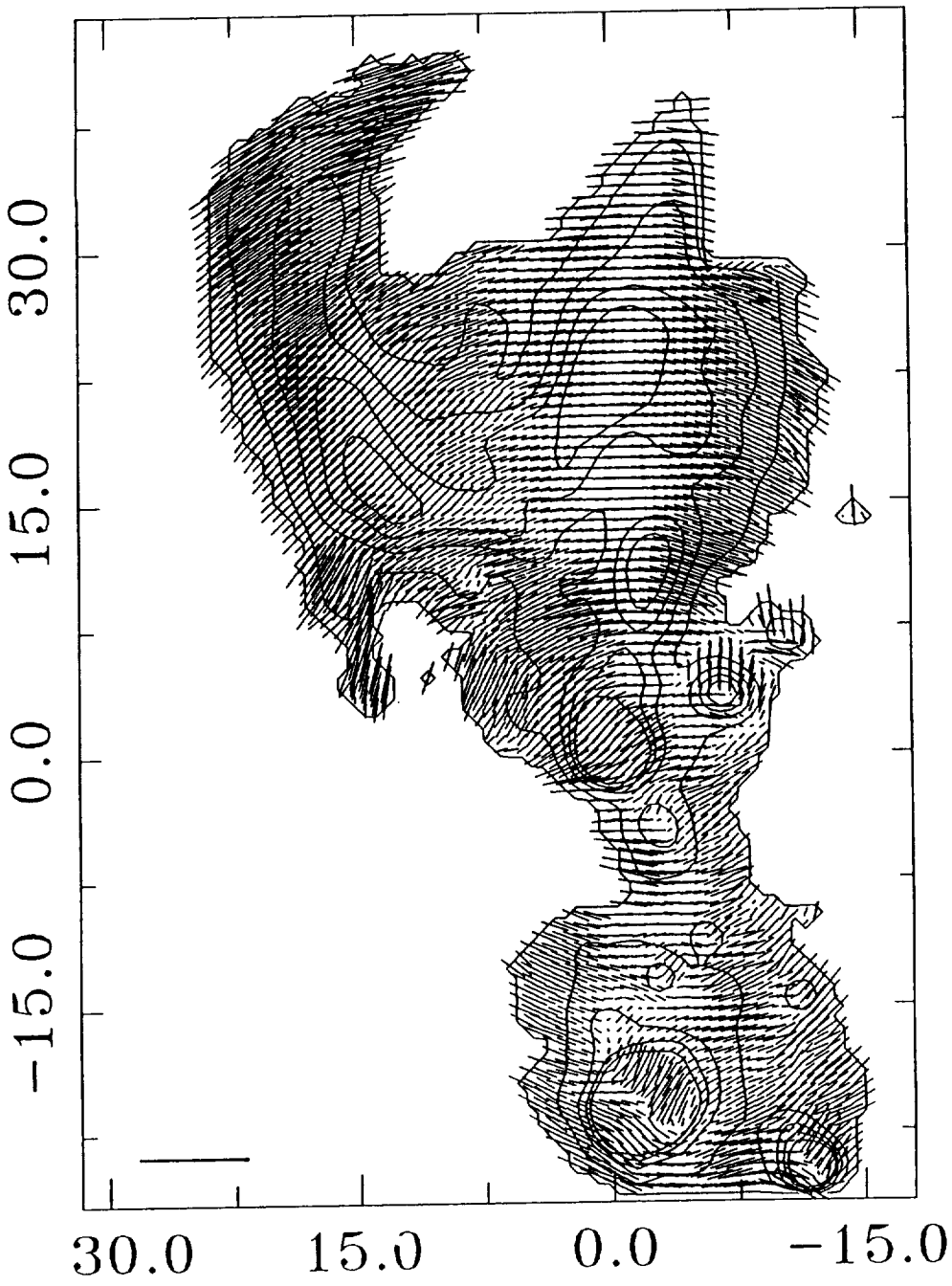

Figure 4: The pattern of linear polarization in the K band for GGD-27. Each line segment represents the percentage linear polarization and the orientation of the electric vector. Note the centro-symmetric pattern.

to be a barred spiral galaxy and there are also clear indications of a non-axisymmetric component in the bulge of M51 itself. The bridge to the companion is much fainter in the IR (relative to the spiral arms) than in the optical suggesting that most of the bridge must be composed of young stars. The contrast in the spiral arms, which should show only the linear response of the stars to the density wave, is (as predicted) less in the IR than the optical, and the arms are smoother and broader than the optical.

5.3 The Galactic Center

Continuous infrared imaging at 2.2 μm at a rate of about 4 frames per second was obtained of the Galactic Center during a unique opportunity when the Moon occulted the source on three occasions visible from Mauna Kea [13,14]. Light curves have been obtained and the imaging photometry data have made it possible to re-interpret aperture photometry observations enabling the components of IRS16 to be distinguished (see the paper by Becklin *et al.*).

In another unique study, the first "velocity-resolved" images of the Galactic Center were obtained using a near-infrared imaging Fabry-Perot interferometer tuned to the Brackett gamma line of hydrogen at 2.166 μm and with a velocity resolution of about 90 km/s; the spatial resolution was seeing-limited at about 1 $\widehat{''}$ [15,16]. The FP was scanned over a velocity range of 1045 km/s in steps of 55 km/s and an IRCAM image of 100s on-chip integration time obtained at each setting. The narrow band Brγ filter isolated one order of the FP and the central step of the scan was tuned to the velocity of Brγ from IRS16. When the individual frames have been calibrated and registered, spectra for each spatial location are generated from cuts through the data cube. This technique can generate 3600 spectra of the Galactic Center region in only 30 minutes. Figure 6 shows a contour plot of the peak Brγ emission over the entire field and some sample spectra from a region 10.5 $\widehat{''}$S and 2.5 $\widehat{''}$W of IRS7. The lower intensity level is 0 on all the spectra while the upper level is self-scaled to the maximum value. The spectra show widely varying line profiles. For example in column 41 the lines display a "red wing" which appears to die away as we move towards row 34 where the lines are narrow (<200km/s) and then re-emerges in the south. Such evidence for multiple kinematic components is found throughout the data.

5.4 Planetary nebulae

Images of a shock-heated toroidal ring of molecular hydrogen have been obtained [17] of the planetary nebula NGC7027 which contrasts dramatically with the optical and radio appearance of this object. The radio maps show a shell structure and the optical image is peculiar and irregular due to extinction by dust. McLean et al. re-classify NGC7027 as a "butterfly" or "bow-tie" planetary nebula most probably in a fairly early stage of formation. A multicolor study of an even younger or "proto-planetary nebula" called M2–9 reveals very clearly a large circumstellar disk [18]. Both these objects are shown in Fig. 7a,b.

5.5 Supernova remnants

Using narrow band filters and the wide-field mode of IRCAM (2.4 $\widehat{''}$ pixel) spectacular molecular hydrogen emission in supernova remnants, such as the Cygnus Loop and the Crab Nebula, has been observed with unexpected results which may indicate the occurrence of non-radiative precursor shocks [19,20]. For the Cygnus Loop, a mosaic of 20 frames covering an area of about 7×7 $\widehat{'}$ of the bright filaments in the north eastern segment of the loop revealed unexpectedly strong H_2 emission; the bright optical lines indicate that the shocks are fast (> 100 km/s) and in gas of moderate density (n $\sim$ 10 cm^{-3}). The H_2 emission is associated with the bright optical emission and shows the same filamentary structure but is generally *displaced* in front of the edge of the optical emission. Most of the H_2 emission comes

ORIGINAL PAGE
COLOR PHOTOGRAPH

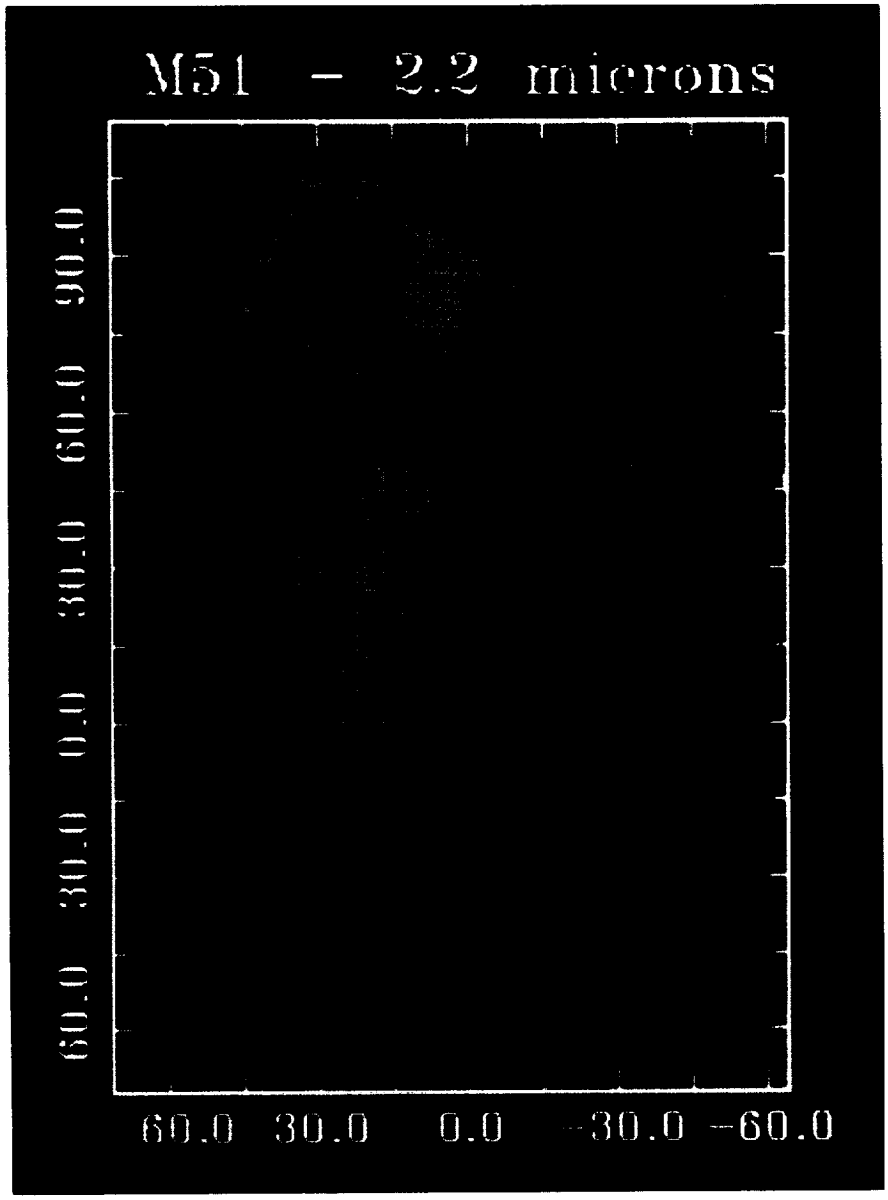

Figure 5: A 2.2 μm (K band) image of the spiral galaxy M51 and its companion. This image is a photometrically-calibrated mosaic of 88 overlapping frames in the 1.2$''$ mode.

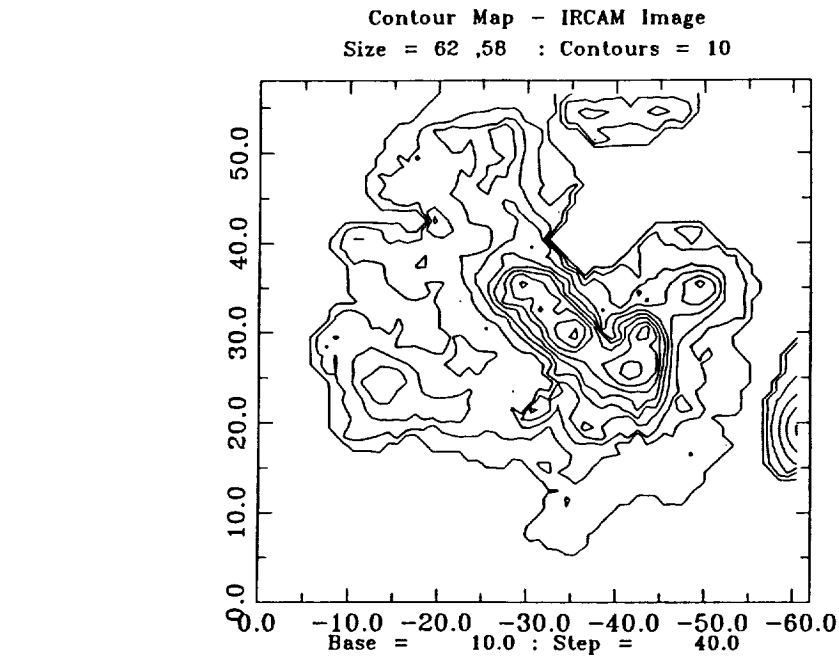

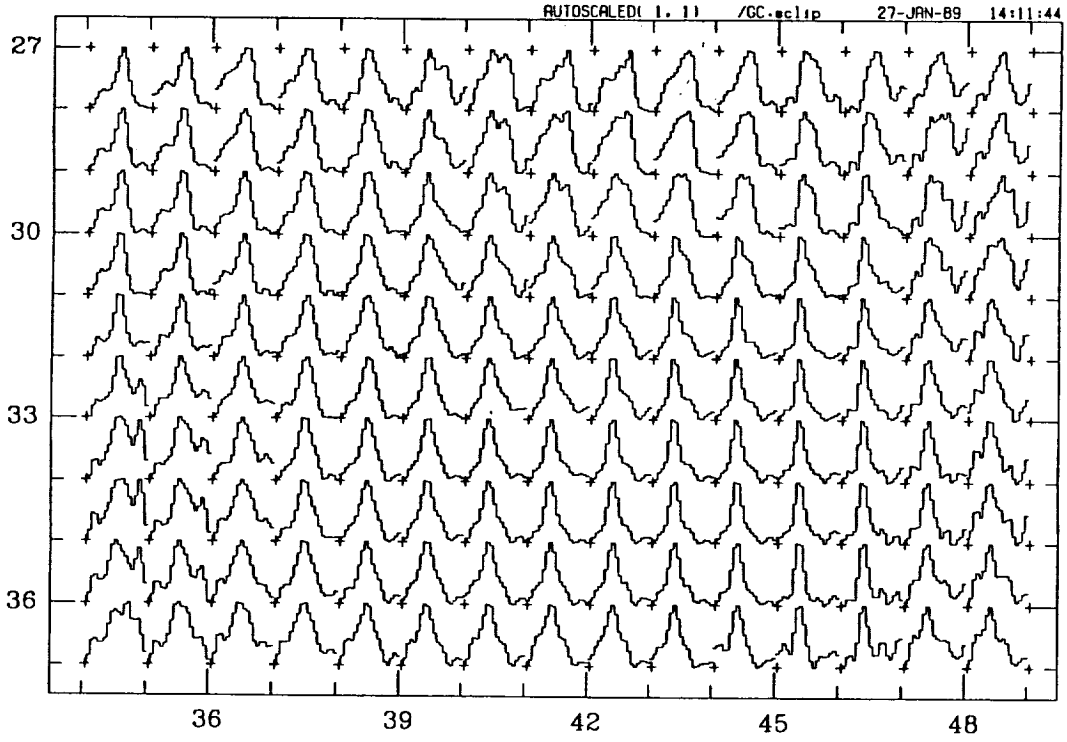

Figure 6: (a) Contour plot of peak Brγ emission in the Galactic Center. (b) A region of the Galactic Center showing the spatial variation of the Brackett gamma line at 2.166 μm with 0.6 arcsecond pixels in 1.0$''$ seeing.

ORIGINAL PAGE
COLOR PHOTOGRAPH

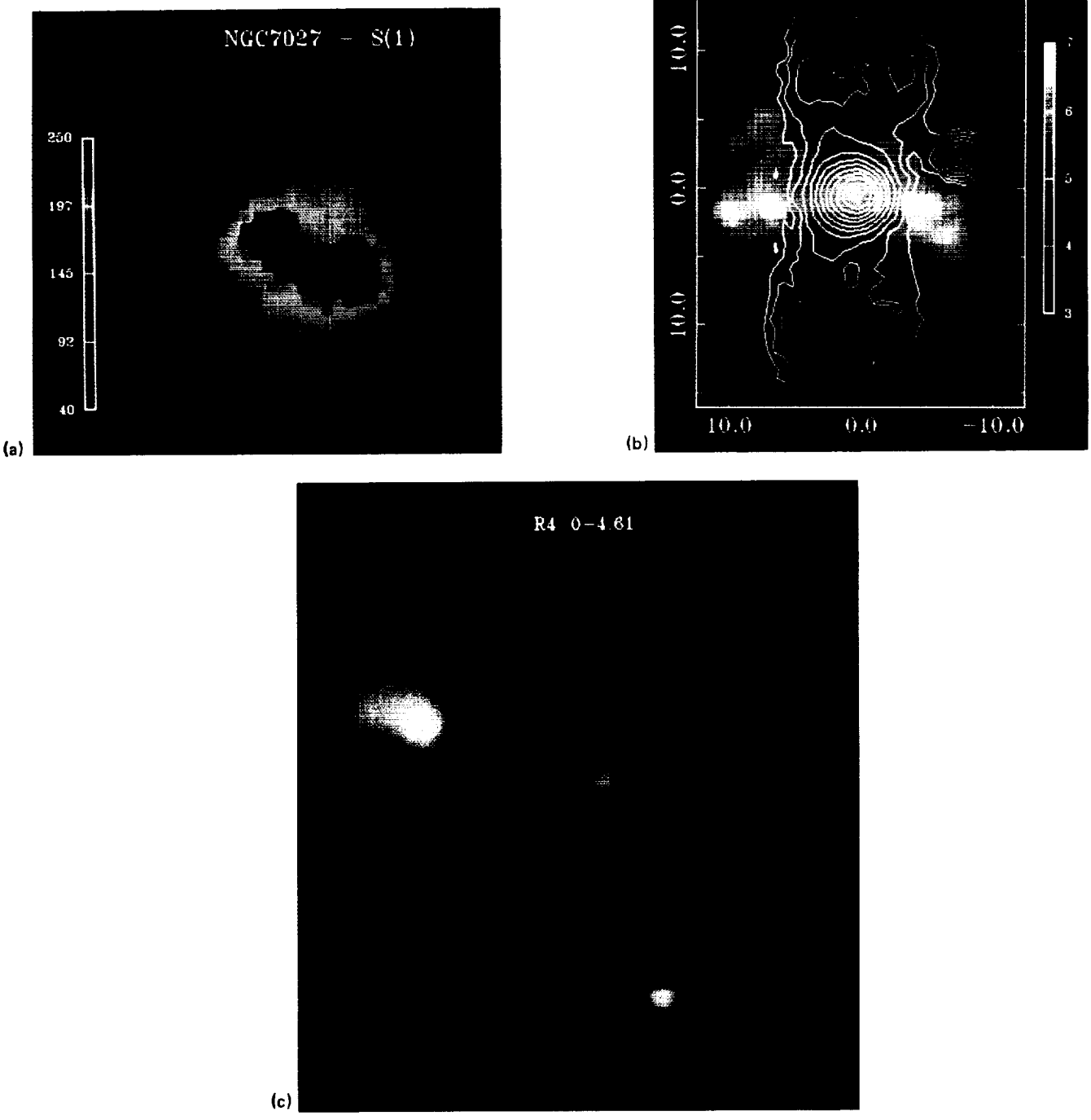

Figure 7: (a) The S(1) v=1-0 emission from the planetary nebula NGC7027. The peak flux in the lobes is about 5×10^{-21}W cm^{-2}; (b) the J-K color map of the proto-planetary object M2–9. The color bar indicates J-K colors in the range 3–7 magnitudes. Overlaid on the map are contours of the J surface brightness; (c) a composite J, H and K image of the star forming region Mon R2 IRS

from a region dominated in the optical by faint, collisionally-excited Balmer emission behind fast (200 km/s) non-radiative shocks propagating into a partially neutral medium. If the pre-shock gas contains a substantial fraction of H_2 rather than HI then the H_2 emission could also be excited in fast adiabatic shocks. Alternatively the H_2 could be excited by UV fluorescence powered by the bright optical shocks.

5.6 Globular clusters

A deep infrared survey of part of the globular cluster M71 was obtained and analysed using the DAOPHOT software package [21]. One strip in the southern part of the cluster has been thoroughly analysed to yield K magnitudes for almost 300 stars using optimised fitting and iterating routines. The best published optical photometry (photographic) does not go as deep and has only 70 stars in the same area. Preliminary V,V-K color-magnitude and B-V,V-K color-color diagrams based on the photographic photometry look very encouraging. Initial experience with the DAOPHOT package suggested that the K zeropoint can be uncertain at the 10% level because of systematic differences in the PSF of the (bright) standard stars used for calibration.

5.7 Deep cosmological surveys

Using a cumulative observation time of almost 12 hours and very careful median-filtering techniques for flat-fielding, the deepest ever infrared images of faint, distant galaxies have been obtained. The limiting magnitude (1 sigma noise) in these studies is around K = 23; the brightness of the infrared background at $2.2\,\mu$m is approximately equivalent to K = 13 per square $\widehat{''}$ - a factor of 10,000! Combined with deep optical CCD images, a population of galaxies at high redshift (z$\sim$3.0) has been discovered with extremely flat spectral energy distributions characteristic of vigorous star formation suggesting that these objects may be "protogalaxies" or galaxies formed earlier but now undergoing a rejuvenation phase [22]. An example of one such object is shown in Figure 8.

6 CONCLUSIONS AND PROSPECTS

These and many other studies barely scratch the surface of what is possible with photometrically calibrated infrared imaging systems. Despite certain limitations, we have been successful in demonstrating flat-fielding accuracies to better than 1 part in 10,000 and relative photometry to better than about 0.01 mag or 1%.

There is no doubt that the 62×58 InSb array from SBRC has been an astoundingly successful device and that it has catapulted infrared astronomy forward at an incredible pace. Even so, the need for larger format detector arrays with lower readout noise and the highest possible quantum efficiency are already urgent.

Acknowledgements It is a pleasure to acknowledge our many colleagues at the Joint Astronomy Centre and at the Royal Observatory, Edinburgh whose efforts have helped to make IRCAM a success. We especially thank Alan Hoffman and David Randall of SBRC, and Mark McCaughrean, John Rayner, Simon Lilly, Andy Longmore, Eric Becklin, James Graham and Joss Bland for many fruitful discussions and suggestions on all aspects of the design, construction and usage of IRCAM at UKIRT.

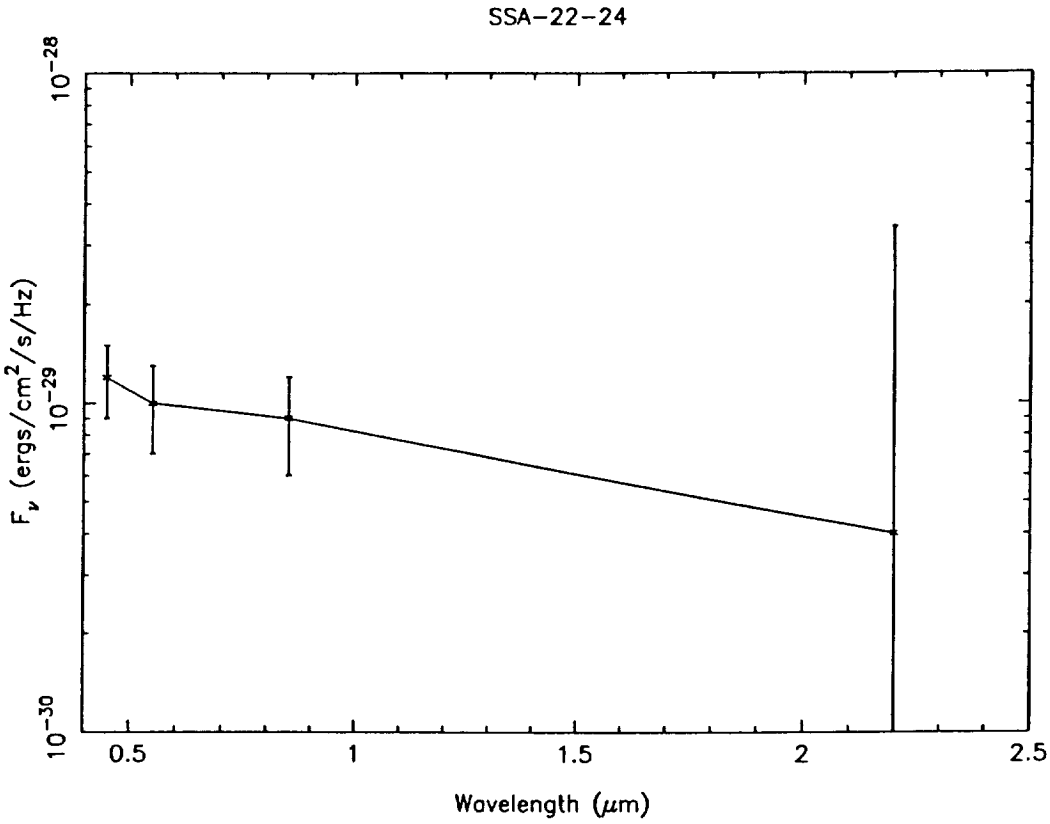

Figure 8: The spectral energy distribution of SSA-22-24 which is a faint galaxy (V=23) at a redshift of about z$\sim$3.5.

REFERENCES AND NOTES

1. I.S. McLean, T.C. Chuter, M.J. McCaughrean and J.T. Rayner, *System Design of a 1-5 μm Infrared Camera*, Proc. SPIE **627**, 430-437 (1986).

2. I.S. McLean, *Results with the UKIRT Camera*, in Infrared Astronomy with Arrays, C.G. Wynn-Williams and E.E. Becklin, eds., Institute for Astronomy, University of Hawaii, 180–192, (1987).

3. I.S. McLean, *Optical or Infrared — the Elusive Boundary*, in Instrumentation for Astronomy; present and future, Proc. Santa Cruz Summer Workshop, Lloyd Robinson, ed., Springer-Verlag, (1988).

4. G. Orias, A.W. Hoffman and M. Casselman, *58×62 InSb focal plane array for infrared astronomy*, in Instrumentation for Astronomy VI, Proc. SPIE, **627**, 408–417, (1986).

5. A.M. Fowler, R.G. Probst, J.P. Britt, R.R. Joyce and F.C. Gillett, *Evaluation of an indium antimonide hybrid focal plane array for ground-based astronomy*, Optical Eng., **26**, 232–240, (1987).

6. M.J. McCaughrean, *The astronomical applications of infrared array detectors*, PhD Thesis, University of Edinburgh, Scotland, (1988).

7. I.S. McLean, *Infrared Astronomy's New Image*, in SKY and TELESCOPE, Vol. **75**, No. 3, 254–258, March (1988).

8. I.S. McLean, *Infrared Astronomy:A New Beginning*, in ASTRONOMY NOW, August (1988).

9. I. Gatley, D.L. Depoy, and A.M. Fowler, *Astronomical Imaging with Infrared Array Detectors*, in SCIENCE, Vol. **242**, 1217–1348, (1988).

10. C.G. Wynn-Williams and E.E. Becklin, Infrared Astronomy with Arrays, Institute for Astronomy, University of Hawaii, Honolulu (1987).

11. R. Garden and A. Russell, in prep. (1989).

12. S. Suzuki-Hayashi, T. Hasagawa, C. Aspin and I.S. McLean, *S106: dispersal of a placental cloud*, submitted Ap. J. (1989).

13. I.S. McLean, C. Aspin, A.J. Longmore and R.I. Dixon, *The January 1987 Galactic Center occultation observed with the UKIRT IR camera, IRCAM*, in Infrared Astronomy with Arrays, C.G. Wynn-Williams and E.E. Becklin eds., Institute for Astronomy, University of Hawaii, 321–325, (1987).
14. Longmore *et al.* in prep (1989).
15. D.L. Depoy, I. Gatley and I.S. McLean, in The Galactic Center, Proc. of UCLA conference (1989).
16. G.S. Wright, J. Bland and I.S. McLean, *An infrared imaging Fabry-Perot study of the Galactic Centre*, in 22nd ESLAB Symposium on Infrared Spectroscopy, Salamanca, (1989).
17. I.S. McLean, I. Gatley, P.W. Brand, S. Hayashi, T. Hasegawa and M. Tanaka, *A molecular toroid in NGC7027*, submitted to Ap.J. (1989)
18. C. Aspin, I.S. McLean and M.G. Smith, *The proto-planetary nebula M2–9*, Astron. Astrophys., **196**, 227-232, (1988).
19. J. Graham, G.S. Wright and A.J. Longmore, *Infrared spectroscopy and imaging of supernova remnants*, in 22nd ESLAB Symposium on Infrared Spectroscopy, (1989).
20. J. Graham, G.S. Wright, J.J. Hester and A.J. Longmore Ap. J. (1989). in preparation
21. A.J. Longmore private communication.
22. L. Cowie, S.J. Lilly, J. Gardner, and I.S. McLean, *A cosmologically significant population of galaxies dominated by very young star formation*, Ap. J Letters, **332**, L29 (1988).
23. C. Aspin, M.J. McCaughrean, I.S. McLean and J.T. Rayner Astron. Astrophys. (1989) in preparation
24. C. Aspin, D.M. Walther and T.G. Geballe, Astron. Astrophys. (1989) in preparation